

MobileSal: Extremely Efficient RGB-D Salient Object Detection

Yu-Huan Wu¹ Yun Liu¹ Jun Xu¹ Jia-Wang Bian² Yuchao Gu¹ Ming-Ming Cheng^{1*}
¹TKLNDST, College of Computer Science, Nankai University ²University of Adelaide

Abstract

The high computational cost of neural networks has prevented recent successes in RGB-D salient object detection (SOD) from benefiting real-world applications. Hence, this paper introduces a novel network, MobileSal, which focuses on efficient RGB-D SOD by using mobile networks for deep feature extraction. The problem is that mobile networks are less powerful in feature representation than cumbersome networks. To this end, we observe that the depth information of color images can strengthen the feature representation related to SOD if leveraged properly. Therefore, we propose an implicit depth restoration (IDR) technique to strengthen the feature representation capability of mobile networks for RGB-D SOD. IDR is only adopted in the training phase and is omitted during testing, so it is computationally free. Besides, we propose compact pyramid refinement (CPR) for efficient multi-level feature aggregation so that we can derive salient objects with clear boundaries. With IDR and CPR incorporated, MobileSal performs favorably against state-of-the-art methods on seven challenging RGB-D SOD datasets with much faster speed (450fps) and fewer parameters (6.5M). The code will be released.

1. Introduction

Salient object detection (SOD) aims to locate and segment the most eye-catching object(s) in natural images. It is a fundamental problem in image understanding and serves as a preliminary step for many computer vision tasks such as image captioning [11], visual tracking [17], content-aware image editing [55], and weakly supervised learning [32]. Current SOD methods are mainly developed for RGB images [28, 30, 41, 53, 64, 67, 68], which are usually hindered by indistinguishable foreground and background textures [5]. To this end, researchers resort to the easily accessible depth information as an important complement to the RGB counterpart, with promising progress in RGB-D SOD [3, 10, 12, 24, 45, 61, 66, 69].

While convolutional neural networks (CNNs) have made brilliant achievements on RGB-D SOD [10, 12, 45, 61, 66,

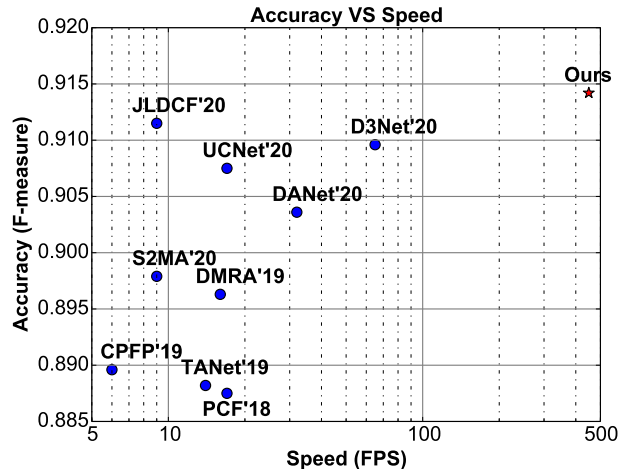


Figure 1. Comparison with state-of-the-art methods (see references in Tab. 2) on the challenging NJU2K [22] dataset. We show higher accuracy and much faster speed.

69], their high accuracy often comes at the expense of high computational costs and large model size. This situation has prevented recent state-of-the-art methods [12, 66] from being applied to real-world applications, especially for those on mobile devices, which are depth accessible, with very limited energy overhead and computational capability. Hence, it is essential to design efficient networks for accurate RGB-D SOD. A naïve solution towards this goal is to adopt lightweight backbones such as MobileNets [19, 48] and ShuffleNets [34, 65] for deep feature extraction, instead of commonly used cumbersome backbones like VGG [49], ResNets [16], and DenseNets [20]. The problem is that lightweight networks are usually less powerful than cumbersome networks on feature representation learning, as widely acknowledged by the research community [19, 34, 48, 65]. This problem would hinder lightweight networks from accurate RGB-D SOD performance.

To overcome this challenge, some researchers resort to the depth information of color images, if leveraged properly, to strengthen the feature representation for efficient RGB-D SOD [45, 66]. Unlike some existing studies [61, 69] that leverage the depth information explicitly, in this paper, we propose an implicit depth restoration (IDR) tech-

*M.-M. Cheng (cmm@nankai.edu.cn) is the corresponding author.

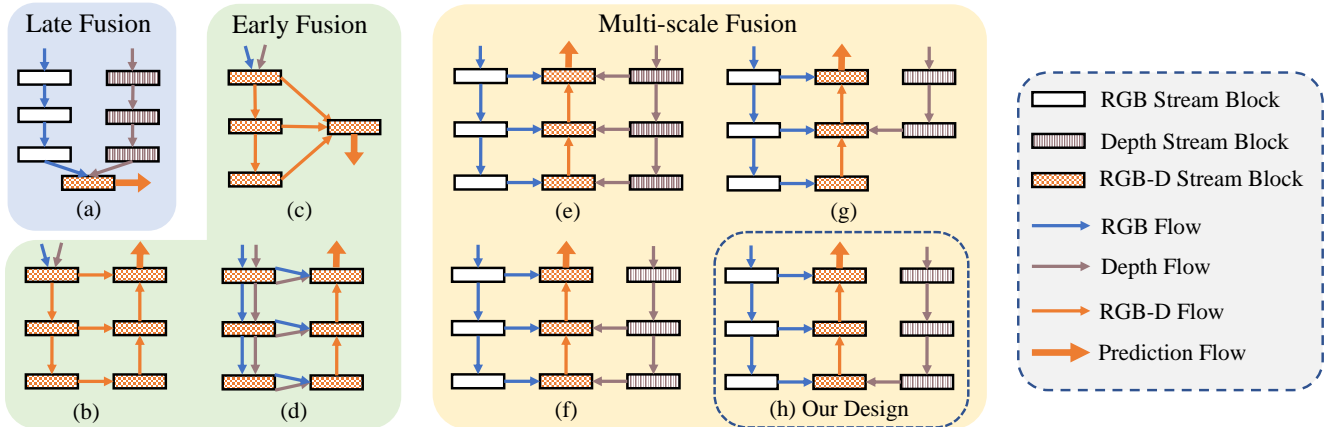


Figure 2. **Architecture differences between existing RGB-D SOD methods (a)-(g) and ours (h).** (a): late fusion. (b)-(d): early fusion. (e)-(h): multi-scale fusion. For efficiency, we only utilize the highest-level depth features on cross-modal fusion. Compared with (a), we leverage multi-scale RGB features. Best viewed in color.

nique to strengthen the feature representation learning of the lightweight backbone network so as to ensure the accuracy of RGB-D SOD in the efficient setting. More importantly, IDR is only adopted in the training phase and is omitted during testing, so it is *computationally free* during the inference stage. Specifically, we enforce our model to restore the depth map from high-level backbone features, through which the representation learning of the lightweight backbone becomes more powerful with extra while important supervision on the depth stream. Besides our IDR module, we propose two more components to ensure the high efficiency: i) we conduct RGB and depth information fusion only at the coarsest level (Fig. 2), because such a small feature resolution (*i.e.*, $1/32$ scale) is essential for reducing computational cost; ii) we propose a compact pyramid refinement (CPR) module to efficiently aggregate multi-scale deep features, for accurate SOD with clear boundaries.

With MobileNetV2 [48] as the backbone network, MobileSal achieves 450fps on a single NVIDIA RTX 2080Ti GPU, tens of times faster than existing RGB-D SOD methods [12, 29, 45, 66]. Extensive experiments on seven challenging datasets demonstrate that MobileSal also performs favorably against state-of-the-art methods (max F-measure of 91.4% and 91.2% on NJU2K [22] and DUTLF [45] datasets, respectively) with fewer parameters (6.5M). Such high efficiency, good accuracy, and small model size would benefit many real-world applications.

In summary, our main contributions include:

- To the best of our knowledge, MobileSal is the first to shed light upon efficient RGB-D SOD by proposing an extremely efficient network with a speed of 450fps.
- To ensure the accuracy of MobileSal, we propose an implicit depth restoration (IDR) technique to strengthen the less powerful features learned by mo-

bile backbone networks.

- To ensure the efficiency of MobileSal on cross-modal fusion, MobileSal fuses RGB and depth information only at the coarsest level and then efficiently aggregates multi-level deep features using a compact pyramid refinement (CPR) module.

2. Related Work

2.1. Salient Object Detection

Benefited from the rapid development of deep CNNs [13, 16, 33, 49] in recent years, CNNs-based SOD methods for RGB images [18, 26, 27, 41, 46, 53, 59, 63, 64, 67, 68] have achieved substantial progress compared with conventional methods [1, 5, 6, 25, 52, 60, 62]. Along this direction, much attention is paid to design various effective strategies to fuse multi-scale features generated by multi-level CNN layers [18, 46, 53, 59, 63, 68]. Some efforts are also spent on exploring the effectiveness of extra boundary information [26, 46, 58, 67]. Despite many success stories, RGB SOD is hindered by indistinguishable foreground and background textures, which can be largely alleviated by incorporating the depth information, *i.e.*, RGB-D SOD.

2.2. RGB-D Salient Object Detection

In terms of the fusion strategy of RGB and depth information, the diagrams of RGB-D SOD architectures can be broadly divided into late fusion [9, 15, 54], early fusion [24, 61, 69], and multi-scale fusion [4, 12, 29, 40, 45, 66]. Late fusion (Fig. 2 (a)) appears at the end of feature extraction and only predicts the result from the fused features [9, 15, 54]. Early fusion directly concatenates the input RGB image and depth map and then derives the saliency

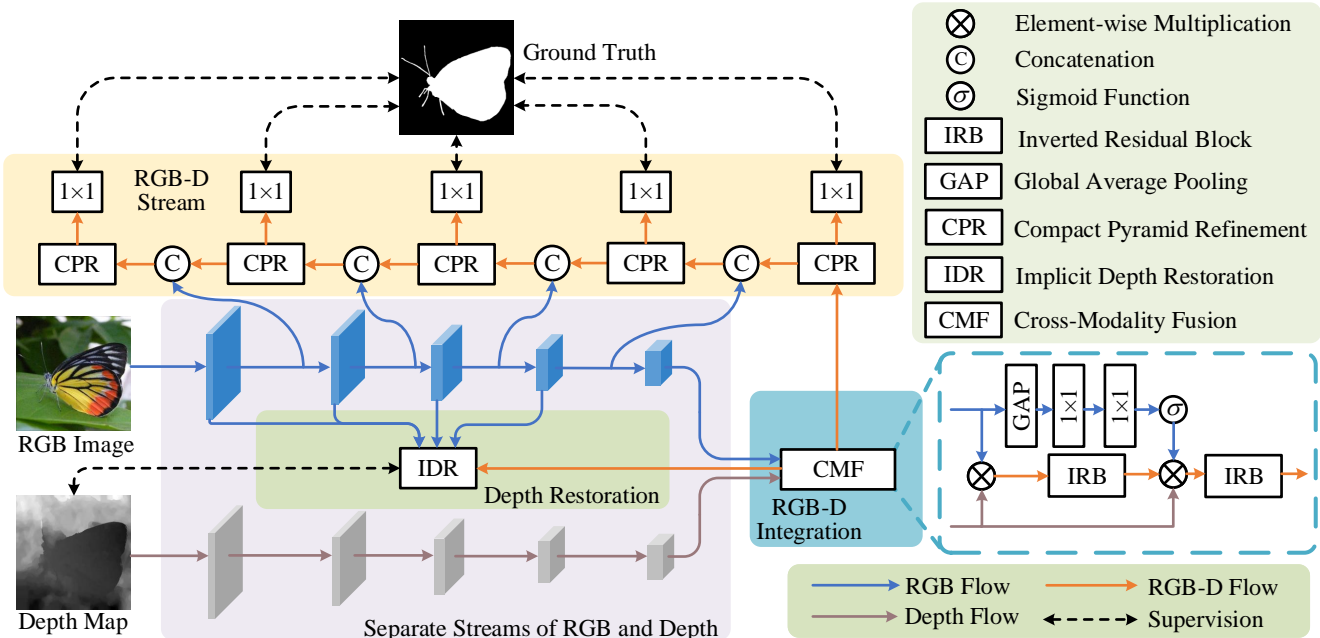


Figure 3. **Overall pipeline of our model.** We fuse RGB and depth information only at the coarsest level and then efficiently do the multi-scale aggregation with CPR module. The IDR branch is to strengthen the less powerful features learned by the mobile networks in a computationally free manner.

map from such RGB-D input using encoder-decoder network [69] (Fig. 2 (b)), hypercolumn network [61] (Fig. 2 (c)), or siamese network [12] (Fig. 2 (d)). Multi-scale fusion first extracts RGB and depth features separately and then aggregates RGB features and depth features at all levels [45] (Fig. 2 (e)), at middle and high levels [4] (Fig. 2 (f)), or at middle levels [40] (Fig. 2 (g)), and then perform the top-down multi-level feature fusion. Although the fusion strategy in Fig. 2 (b) is more efficient, we choose multi-scale fusion to ensure accuracy. To ensure high efficiency, our method only fuses RGB and depth features at the coarsest level in a small resolution (Fig. 2 (h)). IDR is then applied to strengthen the feature representation learning of mobile networks in a computationally free manner.

2.3. Efficient Backbone Networks

Recent growing interests in mobile vision applications have generated a high demand for efficient CNNs. Mobile devices such as autonomous driving vehicles, robots, and smartphones only have limited computational resources, so traditional cumbersome networks, like VGG [49], ResNets [16], and DenseNets [20], are unsuitable for these platforms. To this end, some efficient networks are proposed for image classification, such as MobileNets [19, 48], ShuffleNets [34, 65], MnasNet [50], *etc.* There also emerge some efficient networks for semantic segmentation [35, 36, 42], object detection [51, 57], and ordinary RGB SOD [14, 31]. These efficient networks are with low com-

putational costs and thus flexible for mobile platforms. In this paper, we are the first to shed light upon efficient RGB-D SOD by adopting MobileNetV2 [48] as the backbone for deep feature extraction. Our proposed techniques aim to ensure the SOD accuracy and high efficiency simultaneously in such a lightweight setting.

3. Methodology

In this section, we first provide an overview of our method in §3.1. Then, we introduce the proposed cross-modal feature fusion scheme in §3.2, implicit depth restoration in §3.3, compact pyramid refinement in §3.4. Finally, we present the hybrid loss function in §3.5.

3.1. Overview

The overall architecture of our method is illustrated in Fig. 3. We use RGB and depth streams for separate feature extraction.

RGB Stream. We employ MobileNetV2 [48] as the backbone of our method. To adapt it to the SOD task, we remove the global average pooling layer and the last fully-connected layer from the backbone. For the RGB stream, each stage is followed by a convolutional layer with a stride of 2, and thus feature maps are downsampled into half resolution after each stage. For convenience, we denote the output feature maps for five stages as C_1, C_2, C_3, C_4, C_5 , with strides of $2, 2^2, 2^3, 2^4, 2^5$, respectively.

Depth Stream. Similar to the RGB stream, the depth

stream also has five stages. Since depth maps contain less semantic information than the corresponding RGB images, we build a lightweight depth network with fewer convolutional blocks than that of the RGB stream. Such a design accords with the goal of efficient RGB-D SOD by reducing computational complexity. That is, for each stage, we only use two **Inverted Residual Blocks (IRB)** [48]. In each IRB, we first expand the feature map along the channel dimension by M times via a 1×1 convolution, followed by a depthwise separable 3×3 convolution [19] with the same number of input and output channels. Then, the feature channels are squeezed to $1/M$ via another 1×1 convolution. Here, each convolution is followed by Batch Normalization (BN) [21] and ReLU [38] layers, except for the last 1×1 convolution that only has a BN layer. The final output of the inverted residual block is the element-wise sum of the initial input and the output generated by the above three sequential convolutions. For the first layer in each stage, the stride of the depthwise separable convolution is set as 2, and the number of hidden feature channels is increased if needed. The output feature maps of five stages of the depth stream are denoted as $\mathcal{D}_1, \mathcal{D}_2, \mathcal{D}_3, \mathcal{D}_4, \mathcal{D}_5$, the first four of which have 16, 32, 64, 96 output channels, respectively. \mathcal{D}_5 and \mathcal{C}_5 have the same number of output channels and the same stride.

As shown in Fig. 3, with the outputs of the RGB and depth stream, we first fuse the extracted RGB feature \mathcal{C}_5 and depth feature \mathcal{D}_5 to generate the RGB-D feature \mathcal{C}_5^D . The proposed IDR technique restores the depth map from $\mathcal{C}_1, \mathcal{C}_2, \mathcal{C}_3, \mathcal{C}_4, \mathcal{C}_5^D$, which is supervised by the input depth map to strengthen the feature representation learning. For saliency prediction, we design a lightweight decoder using the CPR module as the basic unit. The output of the decoder at the bottom stage is the final predicted saliency map. More details can be seen in the following sections.

3.2. Cross-Modality of RGB and Depth Features

The depth map reveals spatial cues of color images, which helps distinguish the foreground objects from the background, especially for scenarios with complicated textures. As demonstrated by previous studies [4, 12, 29, 40, 45, 66], proper RGB and depth feature fusion is essential for accurate RGB-D SOD. Our main consideration here is to ensure the high efficiency of our method. Instead of conducting fusion at multiple levels [4, 12, 29, 40, 45, 66], we only fuse RGB and depth features at the coarsest level because the small feature resolution leads to low computational cost.

According to the above analyses, we only fuse the RGB feature map \mathcal{C}_5 and the depth feature map \mathcal{D}_5 . We design a **lightweight Cross-Modality Fusion (CMF)** module for this purpose, as shown in Fig. 3. Intuitively, semantic information mainly exists in the RGB image, and the depth map conveys the prior of depth-smooth regions without object

details. Hence, we adopt depth features as a gate to enhance RGB semantic features by multiplication. Specifically, we first combine the RGB and depth features with an above-mentioned IRB to derive the transited RGB-D feature maps \mathcal{T} , which can be formulated as

$$\mathcal{T} = \text{IRB}(\mathcal{C}_5 \otimes \mathcal{D}_5), \quad (1)$$

where \otimes is the element-wise multiplication operator. Meanwhile, we apply a global average pooling (GAP) layer to \mathcal{C}_5 to get a feature vector, followed by two fully-connected layers to compute the RGB attention vector \mathbf{v} , which can be formulated as

$$\mathbf{v} = \sigma(\text{FC}_2(\text{ReLU}(\text{FC}_1(\text{GAP}(\mathcal{C}_5))))), \quad (2)$$

in which FC and ReLU denote fully-connected and ReLU layers, respectively. The number of output channels of FC_1 and FC_2 is the same as the input. σ indicates the standard sigmoid function. With \mathcal{T} and \mathbf{v} computed, the multiplication of \mathbf{v} , \mathcal{T} , and \mathcal{D}_5 are fed into an IRB, like

$$\mathcal{C}_5^D = \text{IRB}(\mathbf{v} \otimes \mathcal{T} \otimes \mathcal{D}_5), \quad (3)$$

where \mathcal{C}_5^D indicates the output feature map of the CMF module. Note that \mathbf{v} is replicated to the same shape as \mathcal{T} before multiplication. Equ. (3) filters RGB semantic features again by multiplying \mathcal{D}_5 , and the channel attention \mathbf{v} is used to recalibrate the fused features. After the fusion of RGB and depth features, we can derive the backbone features, including the RGB features $\mathcal{C}_1, \mathcal{C}_2, \mathcal{C}_3, \mathcal{C}_4$, and the fused RGB-D feature \mathcal{C}_5^D .

3.3. Implicit Depth Restoration

As widely acknowledged [19, 34, 48, 65], lightweight backbone networks are less powerful in feature representation learning than cumbersome networks. To ensure the accuracy of RGB-D SOD, we consider strengthening the representation learning of mobile networks. We observe that the depth map conveys depth-smooth regions that usually represent objects, object parts, or smooth background, because intuitively, an object or a connected stuff region usually has similar depth. This observation motivates us to use the depth map as an extra supervision source to guide the representation learning, which would help mobile networks restrain the texture changes within objects or connected stuff regions and highlight the difference among them. In this way, the contrast between salient objects and the background will be strengthened too. With this idea, we design an **Implicit Depth Restoration (IDR)** technique. Here, we use the word ‘‘implicit’’ because IDR is only adopted in the training phase and is omitted during testing, making it computationally free for practical deployment.

We continue by introducing how to use $\mathcal{C}_1, \mathcal{C}_2, \mathcal{C}_3, \mathcal{C}_4, \mathcal{C}_5^D$ for the above auxiliary supervision. As shown in Fig. 4 (a),

Figure 4. Illustration of the proposed IDR and CPR. (a) The IDR branch strengthens the less powerful features of mobile backbone network. (b) multi-level deep features are efficiently aggregated by the CPR module. “D-Conv” indicates depthwise separable convolution.

the pipeline of IDR is simple, i.e., just concatenating multi-level feature maps and then fusing them. Specifically, we first apply a 1×1 convolution to squeeze $C_1; C_2; C_3; C_4; C_5^D$ to the same number of channels, 256. Then, the resulting feature maps are resized to the same size, followed by the concatenation of them. A 1×1 convolution changes the concatenated feature map from 1280 channels to 256 channels for saving computational cost. Next, four sequential IRBs are followed to fuse multi-level features so that we can obtain powerful multi-scale features. At last, a simple 1×1 convolution converts the fused feature map to a single channel. With a standard sigmoid function and bilinear upsampling, we can obtain the restored depth map with the same size as the input. The training loss of IDR adopts the well-known SSIM metric [56] to measure the structural similarity between the restored depth map and input one D_g , which can be written as

$$L_{IDR} = 1 - SSIM(D_r; D_g); \quad (4)$$

where SSIM uses the default setting. Note that the above operations are omitted during testing to make IDR free.

3.4. Compact Pyramid Refinement

It is widely accepted that high-level features in the backbone network contain semantic abstract features, while low-level features convey fine-grained details. For accurate SOD, it is essential to fully utilize both high-level and low-level features. There exists a lot of literature on this topic [12, 24, 29, 45, 66], but existing methods usually design cumbersome decoders without consideration of efficiency. Here, our decoder should not only fuse multi-level features effectively but also be efficient as much as possible.

The proposed decoder uses the Compact Pyramid Refinement (CPR) module as the basic unit. For efficiency, CPR uses 1×1 and depthwise separable convolutions [19] instead of vanilla convolutions in previous methods [12, 24, 29, 69]. Since multi-level features exhibit multi-scale representations with the high level corresponding to the coarse scale and vice versa, multi-scale learning would

be necessary for multi-level feature fusion. Hence, CPR adopts a lightweight multi-scale learning strategy to enhance such fusion. Suppose that the input of a CPR module is X . As shown in Fig. 4 (b), CPR first applies a 1×1 convolution to expand the number of channels M by times. Then, three 3×3 depthwise separable convolutions with dilation rates of 1; 2; 3 are connected parallel for multi-scale fusion. This process can be formulated as

$$\begin{aligned} X_1 &= \text{Conv}_{1 \times 1}(X); \\ X_2^{d_1} &= \text{Conv}_{3 \times 3}^{d_1}(X_1); \\ X_2^{d_2} &= \text{Conv}_{3 \times 3}^{d_2}(X_1); \\ X_2^{d_3} &= \text{Conv}_{3 \times 3}^{d_3}(X_1); \\ X_2 &= \text{ReLU}(\text{BN}(X_2^{d_1} + X_2^{d_2} + X_2^{d_3})); \end{aligned} \quad (5)$$

where $d_1, d_2,$ and d_3 are dilation rates, i.e., 1; 2; 3 here, respectively. BN is the abbreviation of batch normalization [21]. A 1×1 convolution is used to squeeze channels to the same number as the input,

$$X_3 = \text{Conv}_{1 \times 1}(X_2) + X; \quad (6)$$

which uses a residual connection for better optimization. The attention mechanism in Equ. (2) is applied to calculate an attention vector v^0 , so that we have

$$Y = v^0 \cdot \text{Conv}_{1 \times 1}(X_3); \quad (7)$$

Equ. (7) uses global contextual information to recalibrate the fused features.

As shown in Fig. 3, at each decoder stage, two feature maps from the top decoder and the corresponding encoder stage first reduce their numbers of channels to half using a 1×1 convolution separately. The results are then concatenated, followed by a CPR module for feature fusion. In this way, our lightweight decoder aggregates multi-level features from top to bottom.

3.5. Hybrid Loss Function

At each decoder stage, we predict the saliency map by sequentially adding a 1×1 convolution with a single chan-

Setting	(a)	(b)	(c)	(d)
Scale	1/8	1/8	1/32	1/8
Data	IDR	GT	GT	GT
Up Type	Bilinear	Bilinear	Bilinear	Nearest
PSNR	22.86	30.17	22.55	24.27
SSIM	.8687	.9194	.8445	.8170

Table 1. Result of our IDR-based depth restoration. The ground truth depth (GT) recovered from different resolutions using different interpolation methods are compared.

nel, a sigmoid function, and bilinear upsampling to the output of the CPR module, as shown in Fig. 3. Hence, we can derive predicted saliency maps $\mathcal{P}_i (i = 1, 2, \dots, 5)$ for five stages, respectively. Let the ground-truth saliency map be \mathcal{G} . The loss of each side-output can be computed as

$$\mathcal{L}_{sal}^i = \text{BCE}(\mathcal{P}_i, \mathcal{G}) + \text{Dice}(\mathcal{P}_i, \mathcal{G}), \quad (8)$$

where BCE denotes binary cross-entropy loss function and Dice represents the Dice loss [37]. The training loss can be formulated as

$$\mathcal{L} = \sum_{i=1}^5 \mathcal{L}_{sal}^i + \lambda \cdot \mathcal{L}_{IDR}, \quad (9)$$

where λ is a balance weight. In the testing phase, \mathcal{P}_1 is the final predicted saliency map.

4. Experiments

Here, we first provide the experimental setup in §4.1. Then, we conduct comprehensive ablation studies in §4.2, and finally, compare with state-of-the-art RGB-D SOD methods in §4.3.

4.1. Experimental Setup

Implementation details. We implement our network in PyTorch [43]. If not specified, we use MobileNetV2 [48] as our backbone. The M values in the depth stream, CPR, and IDR are set to 4, 4, and 6, respectively. We resize both RGB and depth images into 320×320 . We use horizontal flipping and random cropping as the default data augmentation for ablation study. After freezing the designs and parameters, we apply multi-scale training, *i.e.*, each image is resized into [256, 288, 320] in training, but we keep the size of test images unchanged. We use a single RTX 2080Ti GPU for training and testing. The initial learning rate lr is 0.0001, and the batch size is 10. We train our network for 60 epochs. The *poly* learning rate policy is applied, so that the actual learning rate for each epoch cur_epoch is $(1 - \frac{cur_epoch}{60})^{power} \times lr$, where *power* is 0.9. The Adam optimizer [23] is used for optimizing our networks, and the momentum, weight decay, β_1 , and β_2 are set as 0.9, 0.0001, 0.9, and 0.99, respectively.



Figure 5. **Visual comparisons of restored depth maps by IDR with different scales of input depth maps.** Results of the last 3 columns have been upsampled with bilinear interpolation to match the size of input depth map.

Datasets. We conduct experiments on seven widely-used datasets, including NJU2K [22], DUTLF [45], NLPR [44], STEREO [39], DES [7], SSD [70], and SIP [10]. They contain 1985, 1200, 1000, 1000, 135, 80, 927 images, respectively. Following [29, 61, 66, 69], we use 1500 images of NJU2K [22] and 700 images of NLPR [44] for training, and the other 485 images of NJU2K [22] and 300 images of NLPR [44] for testing. Except for DUTLF [45], other datasets are directly used for testing. On the DUTLF [45] dataset, we follow [45, 69] to use 800 images for training and the other 400 images for testing.

Evaluation metrics. Following recent works [2, 3, 61, 66], we adopt two widely-used metrics for evaluation. The first is F-measure F_β , where β is set as 0.3 to emphasize the significance of the precision, as suggested by [1, 45, 66, 69]. We compute the maximum F_β as F_β^{\max} under different thresholds. Higher F_β^{\max} indicates better performance. The second is the Mean Absolute Error (MAE), which is the lower the better. Besides, we report the number of parameters and running time of each method for efficiency analysis.

4.2. Ablation Study

We evaluate each proposed component on the test split of the NJU2K [22] dataset. The results are analyzed below.

Different RGB-D fusions. Tab. 3 shows the results for the RGB-D fusion at different stages. When trained with the IDR branch, fusing RGB and depth features in the coarsest level results in the best performance (No. 6). Fusing RGB and depth features in the last three levels results in the best performance when trained without the IDR branch (No. 11). The IDR branch substantially improves the performance in most cases (No. 3 - 6), and only MAE (fusing

Method	Params (M)	Speed (FPS)	NJU2K [22]		DUTLF [45]		NLPR [44]		STERE [39]		DES [7]		SSD [70]		SIP [10]	
			F_{β}^{\max}	MAE	F_{β}^{\max}	MAE	F_{β}^{\max}	MAE	F_{β}^{\max}	MAE	F_{β}^{\max}	MAE	F_{β}^{\max}	MAE	F_{β}^{\max}	MAE
DESM ₂₀₁₄ [7]	-	-	.7669	.2857	.7281	.2928	.6797	.3160	.7378	.3010	.8000	.3065	.7204	.3130	.7196	.3029
LHM ₂₀₁₄ [44]	-	-	.7034	.2042	.6520	.1624	.6935	.1035	.7519	.1719	.6722	.1138	.6335	.1951	.6344	.1837
ACSD ₂₀₁₄ [22]	-	1	.7495	.1997	.2115	.3195	.6636	.1630	.6818	.1975	.7878	.1627	.7093	.2045	.7883	.1752
DCMC ₂₀₁₆ [8]	-	-	.7589	.1707	.4192	.2323	.7055	.1122	.7895	.1476	.7468	.1111	.7547	.1689	.6800	.1859
CTMF ₂₀₁₇ [15]	-	8	.8572	.0847	.8109	.0953	.8407	.0561	.8476	.0863	.8649	.0554	.7437	.0982	.7175	.1399
DF ₂₀₁₇ [47]	-	-	.8279	.1418	.7283	.1429	.8166	.0796	.7874	.1423	.7961	.0943	.7677	.1432	.7031	.1857
PCF ₂₀₁₈ [2]	133.4	17	.8875	.0592	.7820	.0997	.8635	.0437	.8749	.0635	.8415	.0491	.8333	.0618	.8604	.0706
TANet ₂₀₁₉ [3]	232.4	14	.8882	.0605	.8043	.0920	.8766	.0410	.8775	.0596	.8530	.0460	.8350	.0629	.8493	.0751
CPFP ₂₀₁₉ [66]	69.5	6	.8896	.0533	.7396	.0998	.8878	.0360	.8891	.0514	.8812	.0381	.8013	.0817	.8693	.0637
DMRA ₂₀₁₉ [45]	59.7	16	.8963	.0510	.8869	.0530	.8876	.0315	.8953	.0473	.9074	.0302	.8576	.0586	.8518	.0857
D3Net ₂₀₂₀ [10]	43.2	65	.9096	.0466	.7479	.0988	.9070	.0298	.9040	.0462	.9088	.0314	.8555	.0585	.8803	.0633
JLDCF ₂₀₂₀ [12]	137.0	9	.9115	.0413	.8841	.0533	.9251	.0216	.9131	.0403	.9341	.0205	.8346	.0850	.9028	.0491
S2MA ₂₀₂₀ [29]	86.7	9	.8979	.0539	.8820	.0536	.9097	.0302	.8946	.0514	.9441	.0213	.8779	.0528	.8913	.0575
UCNet ₂₀₂₀ [61]	33.3	17	.9075	.0432	.8359	.0638	.9155	.0250	.9080	.0391	.9364	.0185	.8809	.0491	.8961	.0514
DANet ₂₀₂₀ [69]	26.7	32	.9036	.0469	.8690	.0540	.9075	.0310	.8946	.0481	.9157	.0286	.8779	.0505	.8999	.0543
MobileSal (Ours)	6.5	450	.9142	.0412	.9122	.0410	.9159	.0250	.9062	.0409	.9333	.0210	.8626	.0523	.8985	.0534

Table 2. **Quantitative results on seven challenging datasets.** The best, second best, and third best results are highlighted in **red**, **blue** and **bold**, respectively. Our method achieves the best speed-accuracy trade-off. The subscript of each method is its publication year.

No.	Features to be fused					IDR	F_{β}^{\max}	MAE
	\mathcal{C}_1	\mathcal{C}_2	\mathcal{C}_3	\mathcal{C}_4	\mathcal{C}_5			
1	✓	✓	✓	✓	✓	✓	.9005	.0504
2	✓	✓				✓	.8955	.0482
3	✓	✓	✓			✓	.9003	.0459
4		✓	✓	✓		✓	.9035	.0466
5			✓	✓	✓	✓	.9039	.0448
6					✓	✓	.9081	.0443
7	✓	✓	✓	✓	✓		.8965	.0462
8	✓	✓					.8935	.0474
9	✓	✓	✓				.8974	.0471
10		✓	✓	✓			.8972	.0472
11			✓	✓	✓		.8995	.0479
12					✓		.8972	.0464
13							.8889	.0510

Table 3. **Ablation study for the RGB-D fusion and IDR branch.** Note that the variants of No. 6 and 12 (in **bold**) fuse RGB and depth features only at the coarsest feature level.

Metric	Fig. 2 (b) (Single Stream)		Fig. 2 (h) (Two Streams)	
	IDR ✓	IDR ✗	IDR ✓	IDR ✗
F_{β}^{\max}	0.9018	0.8952	0.9081	0.8972
MAE	0.0473	0.0499	0.0443	0.0464

Table 4. **Comparison of RGB-D fusion strategies** in Fig. 2 (b) and (h). The results of default fusion strategy are with **bold** fonts.

low-level features) degrades (No. 1, 2). This validates the efficacy of the combination of our proposed fusion strategy and the IDR branch. We also compare the used fusion strategy with the early fusion strategy in Fig. 2 (b), which concatenates input RGB image and depth map at the input stage. Although the latter strategy is more efficient, our initial fusion strategy significantly outperforms it (Tab. 4). To ensure accuracy, we use the fusion strategy in Fig. 2 (h).

Depth restoration quality. We explore the restored depth quality of IDR with the widely-used PSNR and SSIM [56] metrics. The scale of the restored depth map in IDR is 1/8 of the input depth map. For comparison, we evaluate the quality of the nearest and bilinear interpolation of input depth map of 1/8 scale. As the IDR branch receives depth features of 1/32 scale, we also report the quality of the bilinear interpolation of depth GT with 1/32 scale. Results are shown in Tab. 1. We observe that the restored depth map is more close to the input depth map than the upsampled 1/32 GT. We also conduct visual comparisons of the above settings in Fig. 5. One can see that the restored depth maps from IDR keep good restoration quality and are with less noise than the upsampled 1/8 GT.

The λ coefficient in the loss function. λ decides the loss weight of the depth restoration loss, as described in Equ. (9). We conduct experiments on our method with different λ settings. The results are shown in Tab. 5. The IDR branch brings substantial improvement to the robustness of our method with different λ . Since the third column achieves the best performance, we adopt $\lambda = 0.3$ as the default setting for training our network.

Depth information and the CMF module. The results in Tab. 6 demonstrate the effects of depth information and the CMF module. Results with depth input are trained with the IDR branch. The providence of depth maps without the CMF module only uses an element-wise multiplication for RGB-D fusion. The Results show that the depth information is very helpful for RGB-D SOD even with a very simple operation. More specifically, we also observe substantial improvement with the CMF module.

Compact pyramid refinement. Tab. 7 shows the results for CPR, where different dilation strategies are used.

No.	1	2	3	4	5	6
λ	0	0.1	0.3	0.5	1	2
F_{β}^{\max}	.8972	.9038	.9081	.9041	.9053	.9037
MAE	.0464	.0452	.0443	.0445	.0429	.0448

Table 5. **Ablation study for λ coefficient selection.** λ is the loss weight of the depth restoration loss. We highlight the results of the default setting in **bold**.

No.	RGB	CPR	Depth	CMF	F_{β}^{\max}	MAE
1	✓				.8532	.0674
2	✓	✓			.8889	.0510
3	✓	✓	✓		.8959	.0473
4	✓	✓	✓	✓	.9081	.0443

Table 6. **Efficacy of CMF.** “RGB” denotes the RGB backbone with the RGB input. “Depth” indicates the network with the depth stream and depth input.

No.	1	2	3	4	5	6
D Rates	1,2,3	1	2	3	1,3,6	1,4,8
F_{β}^{\max}	.9081	.9018	.8934	.8982	.9051	.9027
MAE	.0443	.0459	.0470	.0460	.0452	.0464

Table 7. **Ablation study for the dilation rates of CPR.** “D Rates” means the dilation rates of each depthwise separable convolution.

Method	Ours	JLDCF [12]	UCNet [61]
Input Size	320 × 320	320 × 320	352 × 352
Inference Time (ms)	43 (1×)	7246 (150×)	784 (18×)
Method	D3Net [10]	S2MA [29]	DMRA [45]
Input Size	224 × 224	256 × 256	256 × 256
Inference Time (ms)	677 (15×)	3049 (70×)	2381 (55×)

Table 8. **CPU inference time of different methods.**

We test the default setting (No. 1), single convolution with different dilation rates (No. 2 - 4), and convolutions with sparse combinations of dilation rates (No. 5, 6). The default setting with compact dilation rates significantly outperforms other settings, demonstrating the efficacy of CPR.

4.3. Comparison to state-of-the-art methods

We compare our method with 15 recent state-of-the-art methods on seven widely-used datasets. The saliency maps of other methods are from their released results if provided, otherwise are computed by their released models.

Quantitative comparison. Tab. 2 shows the results. Our method runs at 450fps and only has 6.5M parameters. Other methods are much slower and heavier than our method. For example, JLDCF [12] is 50× slower and has 20× more parameters. UCNet is 26× slower and has 5.5× more parameters. Besides, our method outperforms other methods on NJU2K [22] and DUTLF [45] datasets, and ranks from 2nd to 4th on the other 5 datasets. The above results demonstrate the high efficiency and accuracy of our method.

Qualitative comparison. Fig. 6 shows the results. Due to the limited space, here we only compare our method with CPFPP [66], JLDCF [12], S2MA [29], and UCNet [61] on

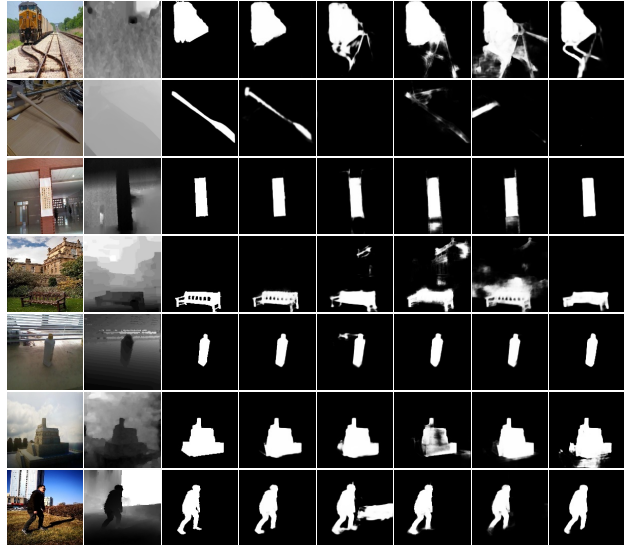


Figure 6. **Qualitative comparison of seven challenging datasets.** The results from top to bottom are from NJU2K, DUTLF, NLPR, STERE, DES, SSD, and SIP datasets, respectively.

all involved datasets. Our method can work well on several kinds of complex scenarios with the noisy depth information, while others may fail in such scenarios. More visual comparisons are attached in the supplementary.

CPU inference time. We test the inference time for different methods in a single core of Intel i7 8700K@3.7GHz CPU. The results are shown in Tab. 8. While the inference time of other state-of-the-art methods (677 ~ 7246 ms) is far from the bar of real-time speed (~50 ms), the CPU inference time of our method can achieve a real-time speed of 43 ms for each RGB-D input.

5. Conclusion

We propose a new method, MobileSal, which aims at efficient RGB-D SOD. Unlike other accurate RGB-D SOD methods, we are the first to shed light upon efficient RGB-D SOD by proposing an extremely efficient network MobileSal with a speed of 450fps. With less powerful features provided by the mobile backbone network, we propose the implicit depth restoration (IDR) technique to strengthen the less powerful features learned by mobile backbone networks. We perform ablation study for the proposed techniques in MobileSal and demonstrate their effectiveness. We conduct experimental comparisons with state-of-the-art methods on seven popular benchmarks. The results show that MobileSal performs favorably against state-of-the-art methods, with fewer parameters and much faster speed. In terms of CPU inference time, our method is 15~150× faster. Our method can serve as a strong baseline for future efficient RGB-D SOD research.

References

- [1] Radhakrishna Achanta, Sheila Hemami, Francisco Estrada, and Sabine Susstrunk. Frequency-tuned salient region detection. In *IEEE CVPR*, pages 1597–1604, 2009. 2, 6
- [2] Hao Chen and Youfu Li. Progressively complementarity-aware fusion network for RGB-D salient object detection. In *IEEE CVPR*, pages 3051–3060, 2018. 6, 7
- [3] Hao Chen and Youfu Li. Three-stream attention-aware network for RGB-D salient object detection. *IEEE TIP*, 28(6):2825–2835, 2019. 1, 6, 7
- [4] Shuhan Chen and Yun Fu. Progressively guided alternate refinement network for RGB-D salient object detection. In *ECCV*, 2020. 2, 3, 4
- [5] Ming-Ming Cheng, Niloy J Mitra, Xiaolei Huang, Philip HS Torr, and Shi-Min Hu. Global contrast based salient region detection. *IEEE TPAMI*, 37(3):569–582, 2014. 1, 2
- [6] Ming-Ming Cheng, Jonathan Warrell, Wen-Yan Lin, Shuai Zheng, Vibhav Vineet, and Nigel Crook. Efficient salient region detection with soft image abstraction. In *IEEE ICCV*, pages 1529–1536, 2013. 2
- [7] Yupeng Cheng, Huazhu Fu, Xingxing Wei, Jiangjian Xiao, and Xiaochun Cao. Depth enhanced saliency detection method. In *Proceedings of international conference on internet multimedia computing and service*, pages 23–27, 2014. 6, 7
- [8] Runmin Cong, Jianjun Lei, Changqing Zhang, Qingming Huang, Xiaochun Cao, and Chungping Hou. Saliency detection for stereoscopic images based on depth confidence analysis and multiple cues fusion. *IEEE Signal Processing Letters*, 23(6):819–823, 2016. 7
- [9] Karthik Desingh, K Madhava Krishna, Deepu Rajan, and CV Jawahar. Depth really matters: Improving visual salient region detection with depth. In *BMVC*, 2013. 2
- [10] Deng-Ping Fan, Zheng Lin, Zhao Zhang, Menglong Zhu, and Ming-Ming Cheng. Rethinking RGB-D salient object detection: Models, data sets, and large-scale benchmarks. *IEEE TNNLS*, 2020. 1, 6, 7, 8
- [11] Hao Fang, Saurabh Gupta, Forrest Iandola, Rupesh K Srivastava, Li Deng, Piotr Dollár, Jianfeng Gao, Xiaodong He, Margaret Mitchell, John C Platt, et al. From captions to visual concepts and back. In *IEEE CVPR*, pages 1473–1482, 2015. 1
- [12] Keren Fu, Deng-Ping Fan, Ge-Peng Ji, and Qijun Zhao. JL-DCF: Joint learning and densely-cooperative fusion framework for RGB-D salient object detection. In *IEEE CVPR*, pages 3052–3062, 2020. 1, 2, 3, 4, 5, 7, 8
- [13] Shanghua Gao, Ming-Ming Cheng, Kai Zhao, Xin-Yu Zhang, Ming-Hsuan Yang, and Philip HS Torr. Res2Net: A new multi-scale backbone architecture. *IEEE TPAMI*, 2020. 2
- [14] Shang-Hua Gao, Yong-Qiang Tan, Ming-Ming Cheng, Chengze Lu, Yunpeng Chen, and Shuicheng Yan. Highly efficient salient object detection with 100K parameters. In *ECCV*, 2020. 3
- [15] Junwei Han, Hao Chen, Nian Liu, Chenggang Yan, and Xuelong Li. CNNs-based RGB-D saliency detection via cross-view transfer and multiview fusion. *IEEE TCYB*, 48(11):3171–3183, 2017. 2, 7
- [16] Kaiming He, Xiangyu Zhang, Shaoqing Ren, and Jian Sun. Deep residual learning for image recognition. In *IEEE CVPR*, pages 770–778, 2016. 1, 2, 3
- [17] Seunghoon Hong, Tackgeun You, Suha Kwak, and Bohyung Han. Online tracking by learning discriminative saliency map with convolutional neural network. In *ACM ICML*, pages 597–606, 2015. 1
- [18] Qibin Hou, Ming-Ming Cheng, Xiaowei Hu, Ali Borji, Zhuowen Tu, and Philip HS Torr. Deeply supervised salient object detection with short connections. *IEEE TPAMI*, 41(4):815, 2019. 2
- [19] Andrew G Howard, Menglong Zhu, Bo Chen, Dmitry Kalenichenko, Weijun Wang, Tobias Weyand, Marco Andreetto, and Hartwig Adam. MobileNets: Efficient convolutional neural networks for mobile vision applications. *arXiv preprint arXiv:1704.04861*, 2017. 1, 3, 4, 5
- [20] Gao Huang, Zhuang Liu, Geoff Pleiss, Laurens Van Der Maaten, and Kilian Weinberger. Convolutional networks with dense connectivity. *IEEE TPAMI*, 2019. 1, 3
- [21] Sergey Ioffe and Christian Szegedy. Batch normalization: Accelerating deep network training by reducing internal covariate shift. In *ACM ICML*, pages 448–456, 2015. 4, 5
- [22] Ran Ju, Ling Ge, Wenjing Geng, Tongwei Ren, and Gangshan Wu. Depth saliency based on anisotropic center-surround difference. In *ICIP*, pages 1115–1119. IEEE, 2014. 1, 2, 6, 7, 8
- [23] Diederik P Kingma and Jimmy Ba. Adam: A method for stochastic optimization. In *ICLR*, 2015. 6
- [24] Chongyi Li, Runmin Cong, Yongri Piao, Qianqian Xu, and Chen Change Loy. RGB-D salient object detection with cross-modality modulation and selection. In *ECCV*, 2020. 1, 2, 5
- [25] Xiaohui Li, Huchuan Lu, Lihe Zhang, Xiang Ruan, and Ming-Hsuan Yang. Saliency detection via dense and sparse reconstruction. In *IEEE ICCV*, pages 2976–2983, 2013. 2
- [26] Jiang-Jiang Liu, Qibin Hou, Ming-Ming Cheng, Jiashi Feng, and Jianmin Jiang. A simple pooling-based design for real-time salient object detection. In *IEEE CVPR*, June 2019. 2
- [27] Nian Liu and Junwei Han. DHSNet: Deep hierarchical saliency network for salient object detection. In *IEEE CVPR*, pages 678–686, 2016. 2
- [28] Nian Liu, Junwei Han, and Ming-Hsuan Yang. Picanet: Pixel-wise contextual attention learning for accurate saliency detection. *IEEE TIP*, 2020. 1
- [29] Nian Liu, Ni Zhang, and Junwei Han. Learning selective self-mutual attention for RGB-D saliency detection. In *IEEE CVPR*, pages 13756–13765, 2020. 2, 4, 5, 6, 7, 8
- [30] Yun Liu, Ming-Ming Cheng, Xinyu Zhang, Guang-Yu Nie, and Meng Wang. DNA: Deeply-supervised nonlinear aggregation for salient object detection. *arXiv preprint arXiv:1903.12476*, 2019. 1
- [31] Yun Liu, Yu-Chao Gu, Xin-Yu Zhang, Weiwei Wang, and Ming-Ming Cheng. Lightweight salient object detection via hierarchical visual perception learning. *IEEE TCYB*, 2020. 3

- [32] Yun Liu, Yu-Huan Wu, Pei-Song Wen, Yu-Jun Shi, Yu Qiu, and Ming-Ming Cheng. Leveraging instance-, image- and dataset-level information for weakly supervised instance segmentation. *IEEE TPAMI*, 2020. 1
- [33] Jonathan Long, Evan Shelhamer, and Trevor Darrell. Fully convolutional networks for semantic segmentation. In *IEEE CVPR*, pages 3431–3440, 2015. 2
- [34] Ningning Ma, Xiangyu Zhang, Hai-Tao Zheng, and Jian Sun. ShuffleNet v2: Practical guidelines for efficient cnn architecture design. In *ECCV*, pages 116–131, 2018. 1, 3, 4
- [35] Sachin Mehta, Mohammad Rastegari, Anat Caspi, Linda Shapiro, and Hannaneh Hajishirzi. ESPNet: Efficient spatial pyramid of dilated convolutions for semantic segmentation. In *ECCV*, pages 552–568, 2018. 3
- [36] Sachin Mehta, Mohammad Rastegari, Linda Shapiro, and Hannaneh Hajishirzi. ESPNetv2: A light-weight, power efficient, and general purpose convolutional neural network. In *IEEE CVPR*, 2019. 3
- [37] Fausto Milletari, Nassir Navab, and Seyed-Ahmad Ahmadi. V-Net: Fully convolutional neural networks for volumetric medical image segmentation. In *2016 fourth international conference on 3D vision (3DV)*, pages 565–571. IEEE, 2016. 6
- [38] Vinod Nair and Geoffrey E Hinton. Rectified linear units improve restricted boltzmann machines. In *ICML*, pages 807–814, 2010. 4
- [39] Yuzhen Niu, Yujie Geng, Xueqing Li, and Feng Liu. Leveraging stereopsis for saliency analysis. In *IEEE CVPR*, pages 454–461. IEEE, 2012. 6, 7
- [40] Youwei Pang, Lihe Zhang, Xiaoqi Zhao, and Huchuan Lu. Hierarchical dynamic filtering network for RGB-D salient object detection. In *ECCV*, 2020. 2, 3, 4
- [41] Youwei Pang, Xiaoqi Zhao, Lihe Zhang, and Huchuan Lu. Multi-scale interactive network for salient object detection. In *IEEE CVPR*, pages 9413–9422, 2020. 1, 2
- [42] Adam Paszke, Abhishek Chaurasia, Sangpil Kim, and Eugenio Culurciello. ENet: A deep neural network architecture for real-time semantic segmentation. *arXiv preprint arXiv:1606.02147*, 2016. 3
- [43] Adam Paszke, Sam Gross, Francisco Massa, Adam Lerer, James Bradbury, Gregory Chanan, Trevor Killeen, Zeming Lin, Natalia Gimelshein, Luca Antiga, et al. PyTorch: An imperative style, high-performance deep learning library. In *NeurIPS*, pages 8026–8037, 2019. 6
- [44] Houwen Peng, Bing Li, Weihua Xiong, Weiming Hu, and Rongrong Ji. RGBD salient object detection: a benchmark and algorithms. In *ECCV*, pages 92–109. Springer, 2014. 6, 7
- [45] Yongri Piao, Wei Ji, Jingjing Li, Miao Zhang, and Huchuan Lu. Depth-induced multi-scale recurrent attention network for saliency detection. In *IEEE ICCV*, pages 7254–7263, 2019. 1, 2, 3, 4, 5, 6, 7, 8
- [46] Xuebin Qin, Zichen Zhang, Chenyang Huang, Chao Gao, Masood Dehghan, and Martin Jagersand. BASNet: Boundary-aware salient object detection. In *IEEE CVPR*, pages 7479–7489, 2019. 2
- [47] Liangqiong Qu, Shengfeng He, Jiawei Zhang, Jiandong Tian, Yandong Tang, and Qingxiong Yang. RGBD salient object detection via deep fusion. *IEEE TIP*, 26(5):2274–2285, 2017. 7
- [48] Mark Sandler, Andrew Howard, Menglong Zhu, Andrey Zhmoginov, and Liang-Chieh Chen. MobileNetV2: Inverted residuals and linear bottlenecks. In *IEEE CVPR*, pages 4510–4520, 2018. 1, 2, 3, 4, 6
- [49] Karen Simonyan and Andrew Zisserman. Very deep convolutional networks for large-scale image recognition. In *ICLR*, 2015. 1, 2, 3
- [50] Mingxing Tan, Bo Chen, Ruoming Pang, Vijay Vasudevan, Mark Sandler, Andrew Howard, and Quoc V Le. MnasNet: Platform-aware neural architecture search for mobile. In *IEEE CVPR*, pages 2820–2828, 2019. 3
- [51] Mingxing Tan, Ruoming Pang, and Quoc V Le. EfficientDet: Scalable and efficient object detection. In *IEEE CVPR*, pages 10781–10790, 2020. 3
- [52] Jingdong Wang, Huaizu Jiang, Zejian Yuan, Ming-Ming Cheng, Xiaowei Hu, and Nanning Zheng. Salient object detection: A discriminative regional feature integration approach. *IJCV*, 123(2):251–268, 2017. 2
- [53] Linzhao Wang, Lijun Wang, Huchuan Lu, Pingping Zhang, and Xiang Ruan. Salient object detection with recurrent fully convolutional networks. *IEEE TPAMI*, 41(7):1734–1746, 2018. 1, 2
- [54] Ningning Wang and Xiaojin Gong. Adaptive fusion for rgb-d salient object detection. *IEEE Access*, 7:55277–55284, 2019. 2
- [55] Wenguan Wang, Jianbing Shen, and Haibin Ling. A deep network solution for attention and aesthetics aware photo cropping. *IEEE TPAMI*, 41(7):1531–1544, 2018. 1
- [56] Zhou Wang, Alan C Bovik, Hamid R Sheikh, and Eero P Simoncelli. Image quality assessment: from error visibility to structural similarity. *IEEE TIP*, 13(4):600–612, 2004. 5, 7
- [57] Ziwei Wang, Ziyi Wu, Jiwen Lu, and Jie Zhou. BiDet: An efficient binarized object detector. In *IEEE CVPR*, pages 2049–2058, 2020. 3
- [58] Runmin Wu, Mengyang Feng, Wenlong Guan, Dong Wang, Huchuan Lu, and Errui Ding. A mutual learning method for salient object detection with intertwined multi-supervision. In *IEEE CVPR*, pages 8150–8159, 2019. 2
- [59] Zhe Wu, Li Su, and Qingming Huang. Cascaded partial decoder for fast and accurate salient object detection. In *IEEE CVPR*, pages 3907–3916, 2019. 2
- [60] Chuan Yang, Lihe Zhang, Huchuan Lu, Xiang Ruan, and Ming-Hsuan Yang. Saliency detection via graph-based manifold ranking. In *Proceedings of the IEEE conference on computer vision and pattern recognition*, pages 3166–3173, 2013. 2
- [61] Jing Zhang, Deng-Ping Fan, Yuchao Dai, Saeed Anwar, Fatemeh Sadat Saleh, Tong Zhang, and Nick Barnes. UC-Net: uncertainty inspired RGB-D saliency detection via conditional variational autoencoders. In *IEEE CVPR*, pages 8582–8591, 2020. 1, 2, 3, 6, 7, 8

- [62] Lihe Zhang, Jianwu Ai, Bowen Jiang, Huchuan Lu, and Xiukui Li. Saliency detection via absorbing markov chain with learnt transition probability. *IEEE TIP*, 27(2):987–998, 2017. [2](#)
- [63] Pingping Zhang, Wei Liu, Huchuan Lu, and Chunhua Shen. Salient object detection with lossless feature reflection and weighted structural loss. *IEEE TIP*, 28(6):3048–3060, 2019. [2](#)
- [64] Pingping Zhang, Dong Wang, Huchuan Lu, Hongyu Wang, and Xiang Ruan. Amulet: Aggregating multi-level convolutional features for salient object detection. In *IEEE ICCV*, pages 202–211, 2017. [1](#), [2](#)
- [65] Xiangyu Zhang, Xinyu Zhou, Mengxiao Lin, and Jian Sun. ShuffleNet: An extremely efficient convolutional neural network for mobile devices. In *IEEE CVPR*, pages 6848–6856, 2018. [1](#), [3](#), [4](#)
- [66] Jiaxing Zhao, Yang Cao, Deng-Ping Fan, Xuan-Yi Li, Le Zhang, and Ming-Ming Cheng. Contrast prior and fluid pyramid integration for RGBD salient object detection. In *IEEE CVPR*, pages 3927–3936, 2019. [1](#), [2](#), [4](#), [5](#), [6](#), [7](#), [8](#)
- [67] Jia-Xing Zhao, Jiang-Jiang Liu, Deng-Ping Fan, Yang Cao, Jufeng Yang, and Ming-Ming Cheng. EGNNet: Edge guidance network for salient object detection. In *IEEE ICCV*, pages 8779–8788, 2019. [1](#), [2](#)
- [68] Xiaoqi Zhao, Youwei Pang, Lihe Zhang, Huchuan Lu, and Lei Zhang. Suppress and balance: A simple gated network for salient object detection. In *ECCV*, 2020. [1](#), [2](#)
- [69] Xiaoqi Zhao, Lihe Zhang, Youwei Pang, Huchuan Lu, and Lei Zhang. A single stream network for robust and real-time RGB-D salient object detection. In *ECCV*, 2020. [1](#), [2](#), [3](#), [5](#), [6](#), [7](#)
- [70] Chunbiao Zhu and Ge Li. A three-pathway psychobiological framework of salient object detection using stereoscopic technology. In *ICCV Workshops*, pages 3008–3014, 2017. [6](#), [7](#)